








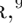


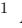



Modest dust settling in the IRAS04302+2247 Class I protoplanetary disk

M. VILLENAVE ¹, L. PODIO ², G. DUCHÊNE ^{3,4}, K. R. STAPELFELDT ¹, C. MELIS ⁵, C. CARRASCO-GONZALEZ ⁶,
V. J. M. LE GOUELLEC ⁷, F. MÉNARD ⁴, M. DE SIMONE ⁸, C. CHANDLER ⁹, A. GARUFI ², C. PINTE ^{10,4},
E. BIANCHI ¹¹ AND C. CODELLA ^{2,4}

¹*Jet Propulsion Laboratory, California Institute of Technology, 4800 Oak Grove Drive, Pasadena, CA 91109, USA*

²*INAF – Osservatorio Astrofisico di Arcetri, Largo E. Fermi 5, 50125 Firenze, Italy*

³*Astronomy Department, University of California, Berkeley, CA 94720, USA*

⁴*Univ. Grenoble Alpes, CNRS, IPAG, F-38000 Grenoble, France*

⁵*Center for Astrophysics and Space Sciences, University of California, San Diego, La Jolla, CA 92093-0424, USA*

⁶*Instituto de Radioastronomía y Astrofísica (IRyA-UNAM), Morelia, Mexico*

⁷*SOFIA Science Center, USRA, NASA Ames Research Center, Moffett Field, CA 94045, USA*

⁸*European Southern Observatory, Karl-Schwarzschild-Str. 2, 85748 Garching, Germany*

⁹*National Radio Astronomy Observatory, PO Box O, Socorro, NM 87801, USA*

¹⁰*School of Physics and Astronomy, Monash University, Clayton Vic 3800, Australia*

¹¹*Excellence Cluster ORIGINS, Boltzmannstraße 2, D-85748 Garching bei München, Germany*

ABSTRACT

We present new VLA observations, between 6.8mm and 66mm, of the edge-on Class I disk IRAS04302+2247. Observations at 6.8mm and 9.2mm lead to the detection of thermal emission from the disk, while shallow observations at the other wavelengths are used to correct for emission from other processes. The disk radial brightness profile transitions from broadly extended in previous ALMA 0.9mm and 2.1mm observations to much more centrally brightened at 6.8mm and 9.2mm, which can be explained by optical depth effects. The radiative transfer modeling of the 0.9mm, 2.1mm, and 9.2mm data suggests that the grains are smaller than 1cm in the outer regions of the disk and allows us to obtain the first lower limit for the scale height of grains emitting at millimeter wavelengths in a protoplanetary disk. We find that the millimeter dust scale height is between 1au and 6au at a radius 100au from the central star, while the gas scale height is estimated to be about 7au, indicating a modest level of settling. The estimated dust height is intermediate between less evolved Class 0 sources, that are found to be vertically thick, and more evolved Class II sources, which show a significant level of settling. This suggests that we are witnessing an intermediate stage of dust settling.

Keywords: Protoplanetary disks (1300); Planet formation (1241); Radiative transfer (1335); Dust continuum emission (412)

1. INTRODUCTION

As the birth place of planets, protoplanetary disks are key to understand the diversity of the observed exoplanet population. Within disks, submicron sized particles grow to large pebbles sizes, that eventually aggregate to form planetesimals or planetary cores (Drazkowska et al. 2022). This process can be accelerated in high dust density regions, such as radial substructures or vertically thin dust layers. While

radial substructures have been detected in numerous disks (Andrews et al. 2018), fewer measurements of the vertical extent of millimeter dust in protoplanetary disks have been performed (e.g., Pinte et al. 2016; Doi & Kataoka 2021; Villenave et al. 2022).

The vertical thickness of dust in a disk is set by the efficiency of vertical settling. This mechanism allows dust particles to concentrate into the midplane, with concentrations that depend on their interaction with the gas (Weidenschilling 1977). Larger particles are expected to be more decoupled from the gas and more affected by vertical settling. These large dust grains

(e.g., mm sized) will thus be more concentrated into the midplane than smaller particles (e.g., μm sized) that remain well mixed with the gas and up to high altitudes (Barrière-Fouchet et al. 2005). In addition, vertical settling efficiency depends on the turbulence level of the disk, and on its evolutionary stage.

Star formation is divided into several classes, where Class 0 corresponds to embedded protostars, Class I objects present both a disk and a prominent envelope around the central star, and Class II only have a disk left (e.g., Andre et al. 2000). Direct measurements of millimeter dust scale height in several Class I/II and Class II disks found that the outer regions are very settled, with a typical scale height of less than 1au at a radius of 100au (Pinte et al. 2016; Villenave et al. 2020; Doi & Kataoka 2021; Villenave et al. 2022; Liu et al. 2022). In contrast, observations of younger systems such as HH212, VLA 1623 West, and L1527, in the Class 0 and 0/I stage, revealed much thicker disks, possibly not affected by vertical settling (Lin et al. 2021; Lee et al. 2022; Michel et al. 2022; Ohashi et al. 2022; Sheehan et al. 2022; Sakai et al. 2017). Further constraints on the evolution of the vertical extent of protoplanetary disks of different evolutionary stages, specifically in the Class I, are important to determine the efficiency of this mechanism with age.

In this work, we focus on the IRAS04302+2247 protoplanetary disk system (hereafter IRAS04302) located in the L1536 cloud in the Taurus star-forming region ($d = 161 \pm 3$ pc, Galli et al. 2019). This disk, classified as Class I by Kenyon & Hartmann (1995), has been the subject of a number of studies at various wavelengths providing useful insights on its structure. The scattered light images (Lucas & Roche 1997; Padgett et al. 1999) show a clear dark lane, indicating the presence of a disk seen almost edge on ($90 \pm 3^\circ$, Wolf et al. 2003), and a bipolar nebula, dominated by a prominent envelope structure. The source was also observed at millimeter wavelengths, both in continuum and in different molecular lines (Wolf et al. 2008; Podio et al. 2020; van’t Hoff et al. 2020; Villenave et al. 2020). The Atacama Large Millimeter Array (ALMA) observations at 2.1mm obtained by Villenave et al. (2020) resolved the minor axis size of the disk (beam size $0''.09 \times 0''.04$) and show that the disk is flared, i.e., with a minor axis width increasing with distance from the star. Here, we present new Karl G. Jansky Very Large Array (VLA) observations at wavelengths between 6.8mm and 66mm. These observations are expected to probe grains that are up to one order of magnitude larger than those probed by previous ALMA observations, which are predicted to be more affected by vertical settling. We present the observations

in Sect. 2 and observational results in Sect. 3. Then, in Sect. 4, we compare 0.9mm, 2.1mm, and 9.2mm observations to a grid of radiative transfer models with the aim to obtain constraints on the vertical and radial distribution of the largest grains in the disk. The results are discussed in Sect. 5, and we conclude this work in Sect. 6.

2. OBSERVATIONS AND DATA REDUCTION

In this section, we present the new VLA observations of IRAS04302 at 6.8mm, 9.2mm, 14mm, 40mm, and 66mm. In addition, we also use previously published photometric data points from Gräfe et al. (2013), and ALMA 0.9mm and 2.1mm observations from Villenave et al. (2020). We refer the reader to Villenave et al. (2020) for details on the calibration of the ALMA observations used in this work.

2.1. VLA Ka data

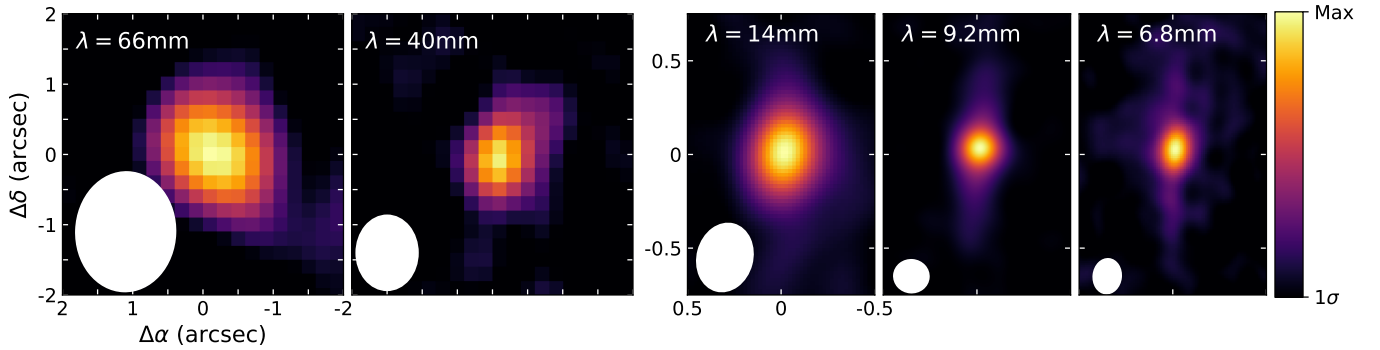
IRAS04302 was observed in the Ka band (9.2mm, Project: 21B-183, PI: Podio) in September and October 2021 with the VLA B configuration for a total of 8.5h on source. In Table 1, we report the observing dates, frequency range, as well as the flux and phase calibrators used for these observations.

We calibrated the raw data using the CASA VLA data reduction pipeline version 6.2.1.7 (CASA Team et al. 2022). Before producing the final images, we identified a mismatch in flux density of a factor 1.07 between observations taken on September 30/October 21 and those taken on October 04/October 21. The observations made on September 30 and October 21 used the flux calibrator 3C147, which is known to be variable (see VLA manual), contrary to 3C286 which was used for the other two observations in Ka band. We thus adjusted the fluxes of the observations from September 30 and October 21 to match those of October 04 and 22 using the `gencal` and `applycal` CASA tasks. To maximize the dynamic range of the image, we then performed phase self-calibration on the observations. Finally, we produced the final continuum image using the `tclean` task, with a briggs weighting (robust 0.5). The resulting continuum beam size and rms are reported in Table 1.

The 9.2mm image resulting directly from the data is presented in Fig. 1. It is likely that the central beam ($\sim 0''.2$) includes contribution from processes other than dust thermal emission, such as free-free emission from ionized jets or disk winds and gyrosynchrotron emission from coronal processes (see Melis et al. 2011, and references therein). Throughout the text we also refer to these processes under the terms “non-dust emission” or “wind/coronal emission”. To subtract such

Table 1. VLA observation log table.

B	λ (mm)	ν (GHz)	Beam size ($''$)	Beam PA ($^\circ$)	RMS ($\mu\text{Jy}/\text{beam}$)	TToS (min)	Project	Observation date	Flux calibrator	Phase calibrator
Q	6.8	40 – 48	0.19×0.15	−6	15.8	45	21B-100	2021/12/18 + 21	3C48	J0431+2037
Ka	9.2	28 – 29 +36 – 37	0.19×0.18	87	4.3	510	21B-183	2021/09/30	3C147	J0426+2327
								2021/10/04	3C286	J0426+2327
								2021/10/21	3C147	J0426+2327
								2021/10/22	3C286	J0426+2327
K	14	18 – 23	0.37×0.29	−14	8.3	10	21B-100	2021/12/18 + 21	3C48	J0431+2037
C1	40	7 – 8	1.07×0.88	0	9.4	8	21B-100	2021/12/18 + 21	3C48	J0431+2037
C2	66	4 – 5	1.70×1.42	−2	10.6	8	21B-100	2021/12/18 + 21	3C48	J0431+2037

 NOTE—B: Observing band; λ : Wavelength corresponding to the average frequency representative of the image; ν : frequency range of the observations; TToS: Total time on source

Figure 1. VLA observations of IRAS04302. The scale bar represents the flux level; its values range between the 1σ level (RMS; Table 1) and the peak flux of each map. This corresponds to a brightness ratio (Max/ 1σ) of 7, 15, 34, 71, and 22, respectively for the 66mm, 40mm, 14mm, 9.2mm, and 6.8mm data. We show the beam size (ellipse) in the bottom left corner of each panel.

non-dust emission, we use other available VLA data (see Sect. 2.2) and follow the method previously implemented by Carrasco-González et al. (2019). We describe the methodology in detail in Appendix A. Ultimately in this paper when modeling the disk (Sect. 4) we consider only the regions outside of 1 beam size to limit the effect of potential variability of processes other than continuum dust emission.

2.2. VLA Q, K, and C data

IRAS04302 was also observed in Q, K, and C bands (Project: 21B-100, PI: Villenave), corresponding to wavelengths between 6.8mm and 66mm, in December 2021 with the VLA in the B configuration. Table 1 presents the frequency range, time on source, observing dates, and calibrators used for these observations. We note that the C band observations were performed with two widely separated basebands of 1 GHz bandwidth each, which we separated into C1 (40mm) and C2 (66mm) to increase the wavelength range probed by these observations. We calibrated the raw data using the CASA pipeline version 6.2.1.7. To increase the sig-

nal to noise of the emission, we produced the final images using the `tclean` task with a natural weighting. We report the beam sizes and rms in Table 1, and show the final images in Fig. 1. Similarly to the observations at 9.2mm, the central regions of the 6.8mm observations are likely affected by processes other than dust thermal emission, which we correct following the methodology described in Appendix A.

3. RESULTS

3.1. Continuum emission, fluxes, and sizes

In Fig. 1, we present the new 66mm, 40mm, 14mm, 9.2mm, and 6.8mm observations without any correction for coronal/wind emission. We find that the 66mm, 40mm, and 14mm observations are unresolved. The spectral index obtained for these three wavelengths (see Sect. 3.2) is inconsistent with dust emission, so we conclude that they are dominated by coronal/wind emission. On the other hand, the 9.2mm and 6.8mm observations are strongly centrally peaked, with detection of extended structure along the disk major axis. The extended component corresponds to thermal emission

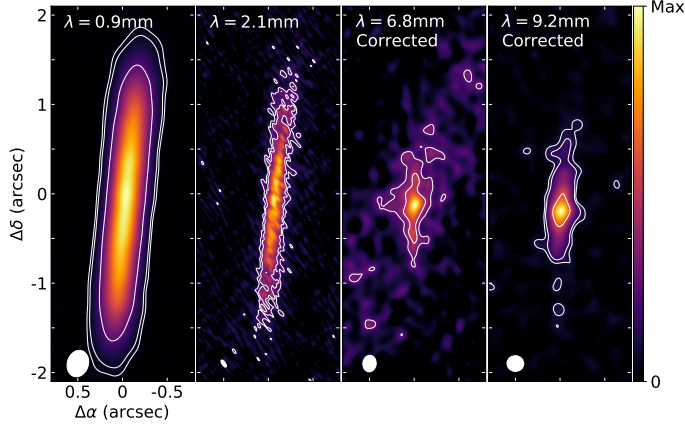


Figure 2. Side by side comparison of the ALMA 0.9mm, 2.1mm and VLA 6.8mm and 9.2mm observations, after correction for emission from processes other than dust continuum emission (Appendix A). The contours indicate emission at the 3, 5, and 20σ levels of each map. The signal to noise of each map ($\text{Max}/1\sigma$) is 83, 17, 11, and 34, respectively for the 0.9mm, 2.1mm and VLA 6.8mm and 9.2mm data. Because of the correction for non-dust emission, the signal to noise of the 6.8mm and 9.2mm data is decreased compared to that reported in Fig. 1.

from the disk, while the central beam is dominated by emission from other processes. In Fig. 2, we show the ALMA 0.9mm and 2.1mm, along with the VLA 6.8mm and 9.2mm observations after correction for processes other than dust continuum emission (see Appendix A). Even after correction, we find that the emission at 6.8mm and 9.2mm is centrally peaked (see also Fig. 3). This could suggest a higher dust concentration or temperature within the inner region of the disk, although caution is needed due to the potential variability of free-free and gyrosynchrotron emission.

We present the flux density of the source at the different wavelengths in Table 2. For the observations where the source is unresolved, namely the 14mm, 40mm, and 66mm observations, we fitted the visibilities by a point source using the `uvmodelfit` CASA task. On the other hand, we estimate the flux density of the extended 6.8mm and 9.2mm observations in the images using an aperture of $0''.8 \times 4''$ ($129 \times 644\text{au}$). We also re-estimate the 2.1mm and 0.9mm fluxes from the ALMA observations of Villenave et al. (2020) using the same aperture, which encompasses all the emission at the four bands. For all wavelengths, we evaluate the uncertainty by taking the quadratic sum of the rms (Table 1) and systematic uncertainty of the observatory (10% for $\lambda \leq 13\mu\text{m}$ and 5% otherwise, see VLA manual).

Table 2. Fluxes and major axis sizes of the VLA and ALMA observations.

λ (mm)	Flux (μJy)	$R_{68\%}$ (")	$R_{95\%}$ (")
0.9	267500 ± 26752	0.90	1.52
2.1	44500 ± 4450^a	0.72	1.51
6.8	$1850 \pm 186^{b,*}$	0.52	1.37
9.2	820 ± 82^b	0.39	1.01
14	294 ± 17	-	-
40	139 ± 11	-	-
66	62 ± 11	-	-

NOTE—The major axis sizes at 6.8mm and 9.2mm were measured on the images corrected for emission from processes other than dust continuum emission. ^(a) The 2.1mm flux reported here is $\sim 20\%$ higher than the flux reported in Villenave et al. (2020), possibly due to differences in aperture sizes. ^(b) After subtracting for non-dust emission, the total flux at 6.8mm and 9.2mm are $1690 \pm 170\mu\text{Jy}$ and $654 \pm 65\mu\text{Jy}$, respectively. ^(*) The flux density of the low signal to noise 6.8mm data strongly depends on the aperture size, likely due to the presence of large scale background structure. It can be decreased by a factor of nearly 2 if the aperture size is smaller.

We estimate the disk size using the cumulative flux technique along the major axis. Previous literature works (e.g., Ansdell et al. 2018; Long et al. 2018), focusing mostly on low- to mid-inclination systems, generally estimated the cumulative flux using elliptical apertures (related to the disk inclination) of increasing radii. However, IRAS04302 is highly inclined and typically unresolved in the minor axis direction, thus using an elliptical aperture to measure the disk size can bias the results. A better approach is to estimate the radius from the cumulative flux obtained from the major axis cut directly (see also Rota et al. 2022, who made a similar choice when measuring the gas size of the edge-on disk around HK Tau B). We calculate the cumulative flux at increasingly larger radii along the major axis cut, where the major axis cut corresponds to a 1-pixel line along the position angle (PA) of the disk and passing by the continuum peak. We then estimate the disk radius $R_{95\%}$ as the radius containing 95% of the total flux, and the effective disk radius as that containing 68% of the total flux ($R_{68\%}$). We note that for 6.8mm and 9.2mm, we use the maps corrected for coronal/wind emission to estimate the disk size. However we checked that using the non-corrected maps only lead to minimal changes in the apparent size, of order $\lesssim 0''.1$. To obtain consistent comparison between the new centimeter range and previous millimeter range observations, we also apply this technique to the previously published ALMA 2.1mm and 0.9mm observations (Villenave et al. 2020). We report

the results in Table 2. We find that both the 68% and the 95% flux radii decrease with wavelength. This is also visible on the top panel of Fig. 3, which shows the major axis profiles of the 0.9mm, 2.1mm, 6.8mm, and 9.2mm observations.

3.2. Spectral indices

The spectral index of millimeter-centimeter emission, defined as α in $F_\nu \propto \nu^\alpha$, can be used to study the dust and optical depth properties within a disk. From our new VLA fluxes at 66mm, 40mm, and 14mm (see Table 2), we estimate a spectral index of $\alpha_{14-66\text{mm}} = 0.97 \pm 0.24$. Using the integrated fluxes reported in Table 2 and from Gräfe et al. (2013), we also estimate a spectral index between 0.9mm and 9.2mm of $\alpha_{0.9-9.2\text{mm}} = 2.54 \pm 0.06$. At longer wavelengths, the spectral index is dominated by coronal/wind emission, while dust dominates at shorter wavelengths.

We also compute the spectral index maps of the centimeter-millimeter emission of IRAS04302. To do so, we first generated 6.8mm and 9.2mm images at the same resolution as the ‘restored’ resolution used by Villenave et al. (2020, $0''.30 \times 0''.24$, see their Table A.1) with the `imsmooth` CASA task. We then generated spectral index maps using the `immath` CASA task on the images at the same resolution. We present the resulting maps in Fig. 4, and the major axis cuts in Fig. 3.

We find that spectral indices increase at larger radii, and also at longer wavelengths. This behaviour is consistent with the expected decrease of optical depth to outer radii. At the center of the disk, emission is presumably very optically thick, and we obtain a spectral index of 2 at nearly all wavelengths. This suggests that the subtraction of the emission from processes other than dust continuum emission (Appendix A) was reasonable, as wind/coronal emission is generally associated with lower spectral index (e.g., Rodmann et al. 2006). When using the longer wavelengths (9.2mm), we see a steeper decrease of the spectral index within $0.5''$ from the center of the disk. This would also be expected in the case of a concentration of larger particles at the center of the disk. However, given the high optical depths expected at these radii, this cannot be clearly concluded from this simple analysis.

4. RADIATIVE TRANSFER MODELING

4.1. Methodology

4.1.1. Model description

To characterize the distribution of large dust in IRAS04302, we model the new 9.2mm VLA and previous 0.9mm and 2.1mm ALMA observations of the system with the radiative transfer code `mcfo`st (Pinte et al.

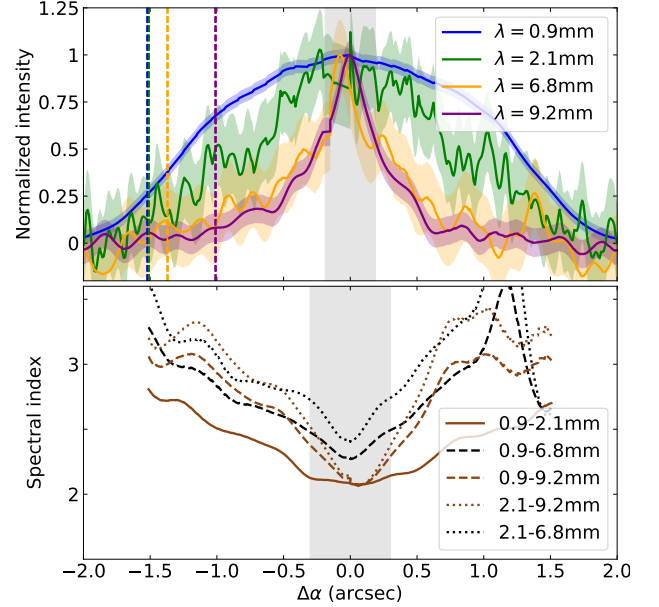


Figure 3. Top panel: Major axis profiles of the 0.9mm, 2.1mm, 6.8mm, and 9.2mm observations (Fig. 2), normalized to their peak. The vertical lines illustrate the location of $R_{95\%}$ (Table 2). Bottom panel: Major axis profiles of the spectral index maps (Fig. 4). The grey region in both panels indicates the region possibly still impacted by coronal/wind emission. It is larger in the bottom plot because the 6.8mm and 9.2mm data were generated at the larger resolution of the 0.9mm image.

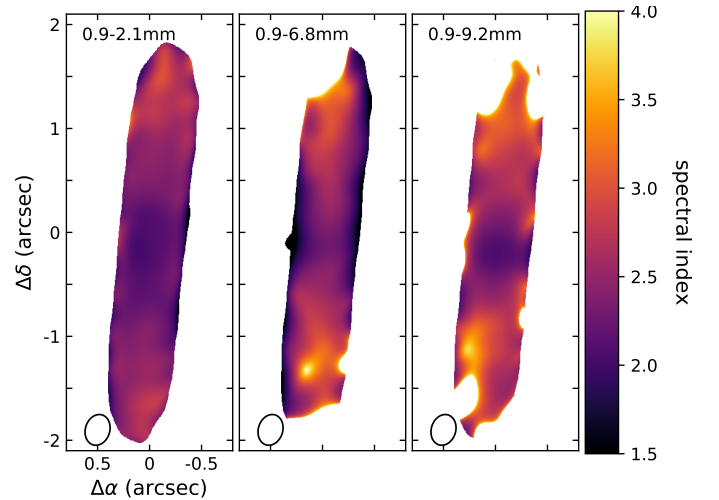


Figure 4. Centimeter and millimeter spectral index maps.

2006, 2009). `Mcfo`st solves the temperature structure using Monte-Carlo methods based on the disk structure and dust properties, properly accounting for scattering effects. We do not consider the 6.8mm data in this analysis because they have a lower signal to noise and same angular resolution as the 9.2mm data (see Table 1).

We assume that the disk is axi-symmetric, smooth, and that the surface density follows a power-law distribution: $\Sigma(r) \propto r^{-p}$, for $R_{in} < r < R_{out}$. The vertical extent of the grains is parameterized such that $H(r) = H_{100au}(r/100au)^\beta$. We assume that the grain size follows a power law distribution such that $n(a)da \propto a^{-3.5}da$.

In addition, as described in Appendix B, we implement a simplified parametrization of vertical settling, namely with a disk represented by a layer of small grains located up to high altitudes in the disk (characterized by $H_{sd,100au}$), and a layer of larger dust more concentrated towards the midplane (characterized by $H_{ld,100au}$, see e.g., Villenave et al. 2022). The complete model, described in Appendix B, also includes an envelope to reproduce the thermal part of the spectral energy distribution.

4.1.2. Fixed and varied parameters

We use a stellar effective temperature of $T_{\text{eff}} = 4500$ K, stellar radius of $3.7R_\odot$ (Gräfe et al. 2013). We fix the inner disk radius to $R_{in} = 0.1$ au, and the outer radius to $R_{out} = 300$ au based on the apparent size of the 0.9mm observations. For the layer of big grains, we fix the minimum grain size to $a_{min} = 10 \mu\text{m}$. Following Gräfe et al. (2013), we also assume that dust grains are composed of a mixture of 62.5% of astronomical silicates and 37.5% of graphite.

We then construct a grid of models by varying several parameters: the dust scale height $H_{ld,100au}$, inclination i , maximum grain size a_{max} , surface density exponent p , flaring exponent β , and dust mass M_{dust} . We report the range of explored parameters in Table 3. We note that we consider only inclinations between 88° and 90° . These values were chosen based on previous modeling of scattered light observations, finding an inclination of $90 \pm 3^\circ$ (Wolf et al. 2003; Lucas & Roche 1997), and based on the shape of the 2.1mm image, which implies an inclination $> 84^\circ$ (Villenave et al. 2020). Our initial modeling trying models between 84° and 88° produced only very bad fits and thus we limited our grid to a minimum inclination of 88° . Our grid consists of $5 \times 3 \times 3 \times 3 \times 4 \times 13 = 7020$ models. For each set of parameters, we compute the 0.89mm, 2.1mm, and 9.2mm images, and convolve the resulting images by the ALMA or VLA 2D Gaussian beam.

4.1.3. Fitting procedure

The goal of this modeling is to reproduce the shape of the millimeter and centimeter emission in order to obtain constraints on the vertical extent of the larger dust particles. Thus, we first build our models by including only a disk region with large grains ($a_{min} = 10 \mu\text{m}$,

Table 3. Overview of the parameter ranges of the grid.

$H_{ld,100au}$	(au)	[1, 3, 4, 5, 6]
i	($^\circ$)	[88, 89, 90]
a_{max}	(μm)	[100, 1000, 10000]
p	(-)	[0.5, 1, 1.5]
β	(-)	[1.06, 1.14, 1.22, 1.3]
$\log_{10}(M_{dust}/M_\odot)$	(-)	[-5.0, -4.75, -4.5, -4.25, -4.0 -3.75, -3.5, -3.25, -3.0, -2.75 -2.5, -2.25, -2.0]

NOTE— $H_{ld,100au}$, i , a_{max} , β , M_{dust} are respectively the large dust scale height at 100au, the inclination, the maximum grain size, surface density exponent, flaring parameter, and the dust mass in the large grain layer.

and varied a_{max} , see Table 3). While adding a layer of smaller grains and envelope allows for a more realistic disk temperature structure, calculating such models is significantly more computationally expensive than when only including the layer of big grains. In Appendix B, we checked that adding such layers does not significantly affect the shape of millimeter/centimeter emission, while allowing a good match in the thermal part of the SED between model and data. Our modeling is thus based on a layer of big grains only.

Our modeling strategy follows 2 key steps, summarized hereafter:

1. For each set of parameters ($H_{ld,100au}$, i , a_{max} , p , β), we first determine the dust mass M_{dust} that offers the best match with the observations along the major axis only. This allows us to obtain optical depths of best-mass models consistent with the observations.
2. We then evaluate the agreement of each best-mass model with the data by considering both the major and minor axis profiles at the three different wavelengths.

For both steps, we determine the best models by considering observations at 0.89mm, 2.1mm, and 9.2mm. For each wavelength, we evaluate the model accuracy in reproducing either the major or minor axis profiles of the data by estimating a χ^2 , defined by:

$$\chi^2 = \sum \frac{1}{n} \left(\frac{F_d - F_m}{\sigma} \right)^2 \quad (1)$$

where F_d and F_m are the respective fluxes of the data and model along the major or minor axis, normalized so that their peak intensity is equal to 1, σ is the normalized rms of the data, and n is the number of pixels along

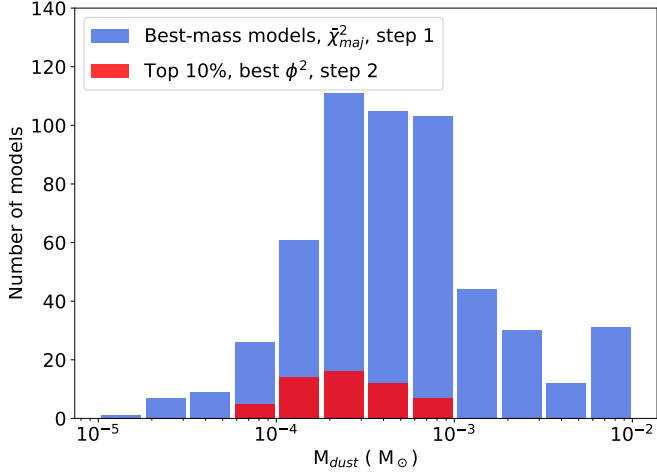


Figure 5. Best dust masses M_{dust} for each combination of $(H_{ld,100au}, i, a_{max}, p, \beta)$ in the grid, based on step 1 (using $\bar{\chi}_{maj}^2$, blue bars). For comparison, the red bars show the dust masses of the 10% best models, based on ϕ^2 . In our initial grid (i.e., before step 1), there are $5 \times 3 \times 3 \times 3 \times 4 = 540$ models in each mass bin (Table 3).

the cut. We note that for the 9.2mm observations, the region within one beam from the central star is not considered, and thus we normalize the data and model major axis profiles to 1 at the distance of one beam from the central star. The accuracy of each model along the major axis is then given by $\bar{\chi}_{maj}^2$, taken as the mean χ_{maj}^2 between 0.89mm, 2.1mm, and 9.2mm. For each set of parameters $(H_{ld,100au}, i, a_{max}, p, \beta)$, step 1 determines the best-mass model (best M_{dust}), which corresponds to that with the lowest $\bar{\chi}_{maj}^2$.

Then, for step 2, we evaluate the agreement of each best-mass model with the data by considering both the major and minor axis profiles at the three different wavelengths. In addition to $\bar{\chi}_{maj}^2$, we evaluate $\bar{\chi}_{min}^2$ along the minor axis direction. We generate minor axis profiles by taking the mean of the cuts at all distances along the major axis (see Villenave et al. 2020), excluding the central region for the 9.2mm comparisons. For each wavelength, we then estimate χ_{min}^2 using equation (1) along the minor axis profiles, and obtain $\bar{\chi}_{min}^2$ as the average between 0.89mm, 2.1mm, and 9.2mm. Finally, the global agreement between our model and the data used in step 2 is obtained by $\phi^2 = \frac{\bar{\chi}_{maj}^2 + \bar{\chi}_{min}^2}{2}$.

4.2. Results

4.2.1. Grid best models

We show the distribution of dust masses for each combination of $(H_{ld,100au}, i, a_{max}, p, \beta)$, as obtained during step 1, in Fig. 5. The median of the distribution is $M_{dust} = 3.2 \times 10^{-4} M_{\odot}$, and the 25% and 75% quar-

tiles respectively reach values of $1.8 \times 10^{-4} M_{\odot}$ and $1.8 \times 10^{-3} M_{\odot}$. For comparison, we also indicate the dust masses of the 10% best models (based on ϕ^2) in this figure. They fall within the range of best dust masses of the distribution from step 1.

In Fig. 5, we can also see that 24 models saturate to the high mass limit of our grid, namely at $M_{dust} = 10^{-2} M_{\odot}$. Those are exclusively models with $H_{ld,100au} = 1$ au, and $i = 88^\circ$, which are typically more centrally peaked than models at higher inclination or with larger scale height. They require a high dust mass to become sufficiently optically thick to reproduce the observations. In fact, nearly all models with this combination of scale height and inclination are extremely high mass. However, it is very unlikely that the dust mass in IRAS04302 is as high or higher than $M_d = 10^{-2} M_{\odot}$, because, assuming a gas to dust ratio of 100, this would imply a star-to-dust mass ratio close to or higher than 1 ($M_{\star} \sim 1.6 M_{\odot}$, Lin et al. in preparation). Thus, this first modeling step indicates that IRAS04302 likely does not have the combination of $H_{ld,100au} = 1$ au and $i = 88^\circ$.

After performing both fitting steps, we find that the parameters of our best model are $H_{ld,100au} = 3$ au, $i = 89^\circ$, $a_{max} = 1$ mm, $\beta = 1.14$, $p = 1.5$, and $M_{dust} = 3 \times 10^{-4} M_{\odot}$. This model is associated to the following metrics: $\phi^2 = 8.1$, $\chi_{maj}^2 = 5.5$, and $\chi_{min}^2 = 10.6$. We show the major and minor axis profiles of this best model in Appendix B, and the maps in Appendix C.

In addition, we also compute the mean and median ϕ^2 , χ_{min}^2 , χ_{maj}^2 values for each $H_{ld,100au}$, i , a_{max} , p , β value of the grid, and show them in Fig. 6. We find that $H_{ld,100au}$ is relatively well constrained, while there are trends for the values of a_{max} and i . Specifically, the models indicate that $1 \text{ au} < H_{ld,100au} < 6 \text{ au}$, and suggest that $a_{max} < 1 \text{ cm}$ and $i > 88^\circ$. For the scale height, we note that $\bar{\chi}_{min}^2$ and $\bar{\chi}_{maj}^2$ favor opposite values, such that the constraint that we obtain is a compromise between the two. On the other hand, the profiles for β and p appear relatively flat and these parameters are thus not constrained.

4.2.2. Radial extent and maximum grain size

As illustrated in Fig. 6, the best maximum grain size in the disk is mostly determined by the major axis profiles. To better understand the effect of grain size on the major axis profiles at our three wavelengths of interest, we present some models in Fig. 7. We chose to show models where only the maximum grain size varies,

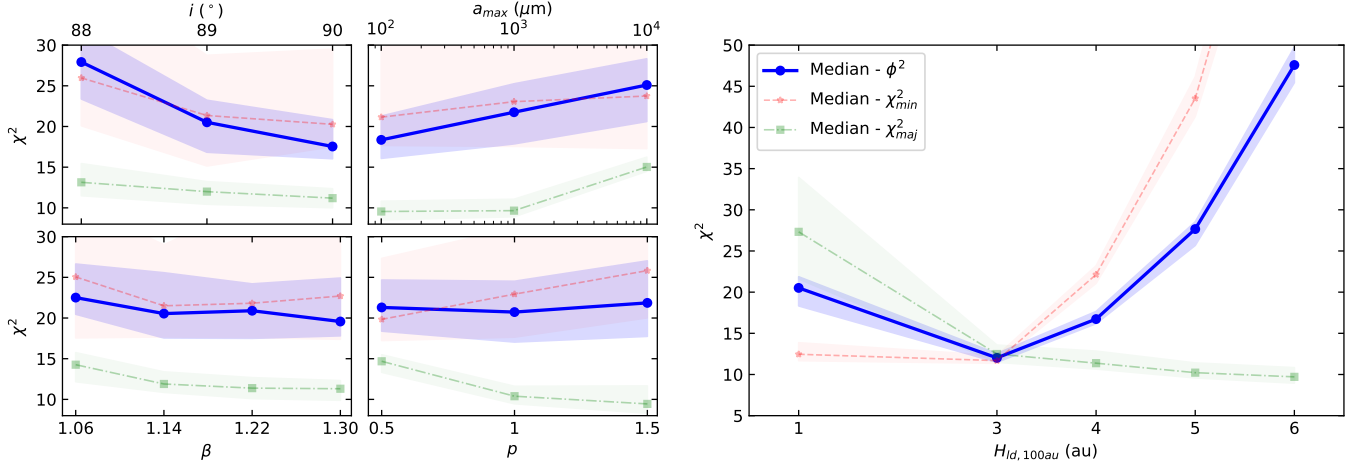


Figure 6. Integrated median ϕ^2 , $\bar{\chi}_{min}^2$, $\bar{\chi}_{maj}^2$ for all best-mass models in our grid. The 40% and 60% percentiles are represented by the shaded contours. Models with $\phi^2 > 25$ are typically bad fits to the data.

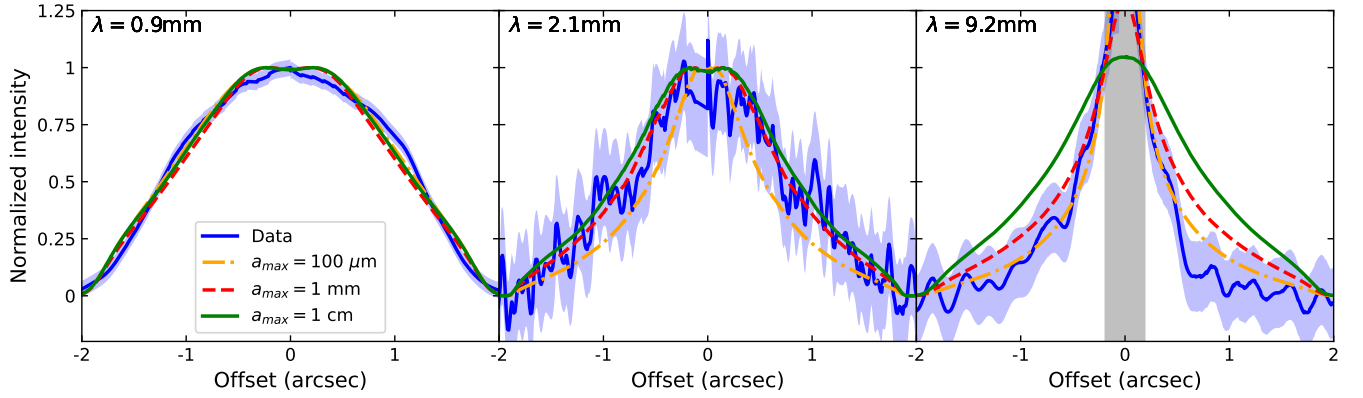


Figure 7. Effect of grain size on the major axis profiles, for models with $H_d = 3au$, $i = 90^\circ$, a_{max} , $p = -1$, and $\beta = 1.14$. The shaded contours show 3 times the rms of the observations. The grey region in the 9.2mm panel indicates the zone potentially contaminated by coronal/wind emission, and not considered in this analysis.

while the other parameters are fixed to $H_{d,100au} = 3au$, $i = 90^\circ$, $p = -1$, $\beta = 1.14$ (the best values from Fig. 6). The corresponding dust masses of each model (as determined in our first modeling step) are $M_{dust} = 10^{-4}M_\odot$ for the models with $a_{max} = 100\mu m$ and $a_{max} = 1mm$, $M_{dust} = 3 \times 10^{-4}M_\odot$ for the model with $a_{max} = 1cm$.

In Fig. 7, we find that the models with $a_{max} = 100\mu m$ and $a_{max} = 1mm$ can simultaneously reproduce the radial extent of the data at 0.9mm, 2.1mm, and 9.2mm, even though radial drift is not included in the modeling. On the contrary, the model with $a_{max} = 1cm$ is unable to reproduce the brightness of the three bands simultaneously. Because of the presence of large grains, the radial profile of that model at 9.2mm is too radially extended to reproduce the data. Most combinations of $(H_{d,100au}, i, p, \beta)$ also exclude a maximum grain size of $a_{max} = 1cm$ as can be seen in Fig. 6. In Appendix C we

show a similar result when considering the $\bar{\chi}_{maj}^2$ values for different pairs of (a_{max}, p) and (a_{max}, i) .

This result indicates that if there are some grains of 1cm in the disk, they can not be well mixed with the gas and extending to the outer disk regions, because the emission would then appear too radially extended at 9.2mm. Such grains of 1cm might however be more concentrated radially than smaller grains, which can not be tested with the current data and modeling. Besides, the models show that if the maximum grain size is between $a_{max} = 100\mu m$ and $a_{max} = 1mm$, optical depths effects alone can be at the origin of the apparent radial segregation between millimeter and centimeter observations. This contrasts with previous radiative transfer modeling results of an other edge-on Class I source CB 26, who found a maximum grain size of 5cm throughout the disk (Zhang et al. 2021).

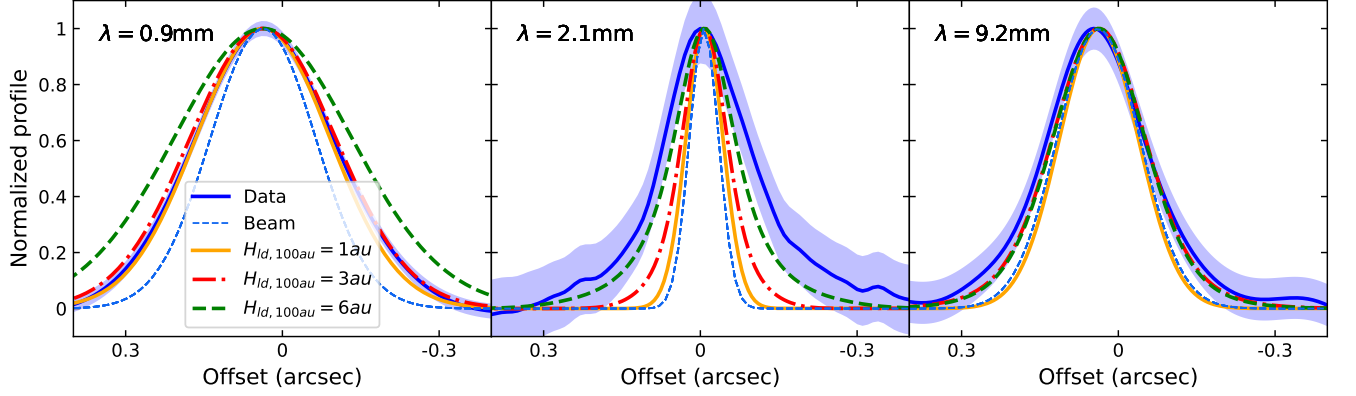


Figure 8. Effect of scale height on the minor axis profiles, for models with $a_{max} = 100\mu m$, $p = -1$, $\beta = 1.14$, and $i = 90^\circ$.

4.2.3. Vertical extent of large dust particles

Our grid models were performed for 5 different scale heights of the large dust grains. In Fig. 8, we present the minor axis profiles of the data and models, integrated over the major axis extent of the disk (see Sect. 4.1.3). We represent models with $a_{max} = 100\mu m$, $p = -1$, $\beta = 1.14$, $i = 90^\circ$, and varying $H_{ld,100au}$. The models with $H_{ld,100au} = 1, 3$ and $6au$ respectively have a dust mass of $M_{dust} = 3 \times 10^{-5}, 10^{-4}$, and $3 \times 10^{-4} M_\odot$. Due to the high inclination of the models, these cuts are dominated by the vertical extent of the disk.

The ALMA 2.1mm image is the most resolved in the vertical direction (Villenave et al. 2020), it is thus the wavelength that is expected to be able to provide most constraints on the vertical extent of the disk. Indeed, we find that while the 1au and 3au models correctly match the respectively marginally resolved and unresolved minor axis profiles of the ALMA 0.9mm and VLA 9.2mm images, they appear to be too vertically thin to reproduce the 2.1mm images. In contrast, we find that the ALMA 0.9mm minor axis profile is not well reproduced by the models with scale height of 6au which appear too vertically extended to match the profiles. As shown in Fig. 6, the best compromise between all bands is achieved for a scale height of 3au, while models with 1au or 6au of scale height can be excluded as they are unable to reproduce either the 2.1mm or the 0.9mm minor extent. In Appendix C, we show that these constraints on the large dust vertical extent are similar for the different inclinations and flaring exponents in our grid. In particular, we emphasize that while the models shown in Fig. 8 have an inclination of 90° , our grid also explored less inclined disks and allowed us to exclude the possibility of IRAS04302 being both less inclined (88° of inclination) and very settled (see Sect. 4.2.1).

Up to here, we focused on the minor axis cut averaged over the full disk. However, Villenave et al. (2020) previously identified that the minor axis size of IRAS04302, measured at 2.1mm, increases with radius. Now, we present the impact of different parameters on the variation of the minor axis extent at different distances from the central star. Following Villenave et al. (2020), we fitted a Gaussian to the minor axis profiles obtained at a different locations. We plot the resulting full width half maximum (FWHM) in Fig. 9 for two sets of models varying either $H_{ld,100au}$ or β . In the two figures, we fix $i = 90^\circ$, $a_{max} = 100\mu m$, $p = -1$. Then the top figure shows the impact of the dust scale height on the minor axis size variation, for $\beta = 1.14$, and the bottom figure shows the effect of flaring on the shape of the minor axis size variation, for $H_{ld,100au} = 6au$ ¹.

We find that while the $H_{ld,100au} = 1au$ model does not show any clear variation of the minor axis size with respect to the distance to the star, every other model does. The model with a dust scale height of 6au provides the best match to the profile and absolute value. On the other hand, the bottom part of Fig. 9 shows that the impact of the flaring exponent is less important than the impact of the scale height. For the range of flaring values explored within our grid and a dust scale height of 6au, all models are consistent with the data within the uncertainties, which does not permit to constrain the flaring of the large dust particles in this system.

To summarize, using a grid of radiative transfer models, we are able to constrain the scale height of the large grains in the Class I IRAS04302. We find that it is of a

¹ The models with varying flaring respectively have a dust mass of $M_{dust} = 3 \times 10^{-4}$ for $\beta = 1.06$ and 1.14 , and $M_{dust} = 3 \times 10^{-4} M_\odot$ for $\beta = 1.22$ and 1.3 . Those with varying scale height are the same as in Fig. 8, and the model with $H_{ld,100au} = 4au$ has a dust mass of $M_{dust} = 2 \times 10^{-5} M_\odot$.

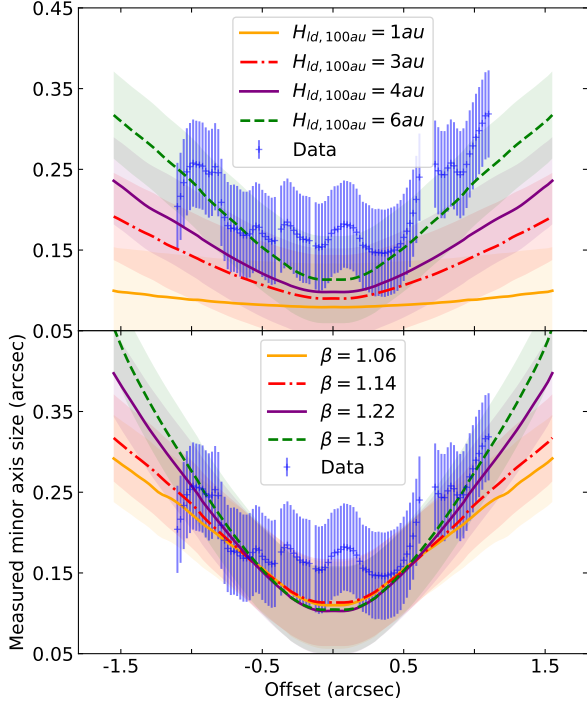


Figure 9. *Top:* Minor axis size as a function of radius of the 2.1mm data and models for $\beta = 1.14$ and varying $H_{ld,100au}$. *Bottom:* Minor axis size as a function of radius of the 2.1mm data and models with $H_{ld,100au} = 6au$, and varying β . Shaded regions show the beam size in the direction of the minor axis cuts.

few astronomical units at a radius of 100au, where values lower than 1au and higher than 6au are excluded by our analysis. We obtain an upper limit consistent with the results of Lin et al. (in preparation), who modeled high angular resolution 1.3mm observations of IRAS04302, and also consistent with previous modeling results from Gräfe et al. (2013), using vertically unresolved millimeter data. The flaring exponent β of the millimeter disk could however not be constrained as its effect are minimal on the minor axis profile radial variation.

We note that no model is able to simultaneously reproduce the 0.9mm and 2.1mm data (see Fig. 8). We suggest that this might be due to the simplifying assumptions that we made for our modeling, namely that we consider fully mixed grains without substructures, that we use a unique maximum grain size, and/or that we determine the dust mass by simultaneously reproducing the major axis profiles of the 0.9mm, 2.1mm, and 9.2mm observations. In particular, our results might suggest that the optical depth change between 0.9mm and 2.1mm is less than what is assumed in the models, such that the 0.9mm image could appear less vertically extended. Besides, the 0.9mm image is also only marginally resolved in the vertical direction, such

that further observations at higher angular resolution would allow to further constrain the vertical extent of large dust in IRAS04302. We note that Lin et al. (in preparation) estimated a dust scale height of about 6au at 100au when working on independent observations of IRAS04302 at 1.3mm with high angular resolution. Their constraints indeed appears more consistent with our results based on our most resolved observation (2.1mm) than from the constraints based on the less resolved 0.9mm image.

5. DISCUSSION

5.1. Dust and gas vertical extent in IRAS04302

In Sect. 4.2.3, we found that the large dust scale height is constrained within $1au < H_{ld,100au} < 6au$. This result can be compared to the gas scale height that we estimate in Appendix B. We used the midplane temperature of our best model to which we added an envelope and a disk layer of small grains to obtain a better representation of the disk temperature structure. We obtained a midplane temperature of 21 K at 100au from the central star², which translates into a gas scale height of $H_{g,100au} \sim 7au$, for a stellar mass of $M_\star = 1.6M_\odot$ (Lin et al. in preparation). The gas scale height appears to be slightly larger than our upper limit of the large dust scale height, suggesting that there is at least some modest amount of vertical settling occurring in the Class I IRAS04302, in agreement with previous conclusions by Gräfe et al. (2013).

From the difference of scale height between the gas and the millimeter dust grains, we can also estimate the degree of coupling of dust with gas, parameterized by the α/St ratio, where St is the Stokes number and α the turbulence parameter. Indeed, assuming that turbulence balances gravity, for grains in the Epstein regime ($St \ll 1$) and under the assumption of $z \ll H_g$, the dust scale height can be written as:

$$H_d = H_g \left(1 + \frac{StSc}{\alpha} \right)^{-1/2} \quad (2)$$

with Sc the Schmidt number, the ratio between turbulent viscosity and turbulent diffusivity. Following previous studies (Dullemond et al. 2018; Rosotti et al. 2020; Villenave et al. 2022), we assume $Sc = 1$, which is valid for particles with $St \ll 1$ (Youdin & Lithwick 2007, see also Johansen & Klahr 2005). For $H_{ld,100au} > 1au$, and $H_g \sim 7au$, we find that $[\alpha/St]_{100au} > 2 \times 10^{-2}$. This

² This temperature is in perfect agreement with the location of the CO snowline by van't Hoff et al. (2020) based on the disappearance of CO from the midplane at 100au (see also Podio et al. 2020).

value is higher than previous estimates on Class II systems (Table 4), which we discuss in Sect. 5.2.

5.2. Comparison with other systems

We now aim to look for any trend of variation of settling efficiency with different parameters, such as stellar mass, disk outer radius, and time. In Table 4, we compiled various parameters for 7 disks of different evolutionary stage with constraints on large dust vertical height (HH212, L1527, VLA 1623 W, IRAS04302, HL Tau, HD163296, Oph163131, Lin et al. 2021; Sheehan et al. 2022; Ohashi et al. 2022; Nakatani et al. 2020; Michel et al. 2022; Pinte et al. 2016; Doi & Kataoka 2021; Liu et al. 2022; Villenave et al. 2022).

The stellar masses gathered in Table 4 are all dynamical estimates based on gas Keplerian rotation. For the Class I and II disks, the abundant ^{12}CO lines were used, while rarer species such as C^{17}O , HCO^+ or SO were considered for the more embedded Class 0 protostars (see references in Table 4). We also recalculated the mass accretion rates of the least evolved systems (HH212, L1527, VLA 1623 W, IRAS04302) based on their bolometric luminosity using $\dot{M}_{acc} = \frac{L_{bol} R_\star}{GM_\star(1-R_\star/R_{in})}$ (Gullbring et al. 1998), assuming that the bolometric luminosity is dominated by the accretion luminosity. We assume a stellar radius of $R_\star = 2R_\odot$ (Lee 2020), and an inner radius of the accretion disk of $R_{in} = 5R_\star$ (Gullbring et al. 1998). For HD163296 and HL Tau, we report estimates based on the UV excess or HI recombination line luminosity, and we note that no clear sign of accretion were found in the spectra of Oph163131 (Flores et al. 2021). Finally, the last column of Table 4 reports the dust height of the different systems. For the most evolved sources, specific radiative transfer modeling were performed, allowing to quantify the vertical extent of large dust particles and to compare it with that of the gas (Pinte et al. 2016; Doi & Kataoka 2021; Liu et al. 2022; Villenave et al. 2022; Wolff et al. 2021). On the other hand, for the younger Class 0 systems, determining the gas height is complex due to the presence of a dense envelope and the different papers did not provide quantitative measurement of the gas and dust scale height. Nevertheless, using radiative transfer, geometrical analysis in the uv-plane, or by measuring the apparent size in the image plane, the authors argued that the young disks of HH212, L1527, and VLA 1623 W are geometrically thick, and possibly not affected by vertical settling (Lin et al. 2021; Sheehan et al. 2022; Ohashi et al. 2022; Michel et al. 2022).

From Table 4, we find that the millimeter dust height appears to correlate with the evolutionary class. In particular, the Class I IRAS04302 appears less settled

than Class II and I/II disks (HD163296, Oph163131, HL Tau). In addition, while we identified at least moderate level of settling in IRAS04302, previous studies of younger Class 0 and 0/I systems (HH212, L1527, VLA1623W) suggested that settling did not occur at all in these young sources. Our results thus seems to support an evolution of settling efficiency with time.

In Table 4, we also find that the younger sources have the least massive stars and least extended disks, which might impact the settling efficiency. To investigate the differences in dust height between the disks, we estimate the timescale for settling under simple assumptions. When only the thermal speed of molecules and vertical settling are considered, in other words in the absence of vertical turbulence and infalling material, the timescale for settling is given by Armitage (2015):

$$t_{\text{settle}} = \frac{\rho}{\rho_m} \frac{v_{th}}{a} \frac{1}{\Omega_K^2} \propto \rho \frac{\sqrt{T}}{a} \frac{R^3}{M_\star} \quad (3)$$

where ρ_m is the dust material density, ρ the gas density, a is the particle size, $v_{th} = \sqrt{8k_B T / \pi \mu m_H}$ is the thermal speed of the molecules, and $\Omega_K = \sqrt{GM_\star / R^3}$ the disk rotation frequency, which depends on the stellar mass (M_\star) and the local radius (R). The settling timescale strongly depends on the radius, particle size, stellar mass, and gas density. Specifically, settling is expected to be faster for larger particles, larger stellar mass, and at the inner regions of the disk. If they were in the same evolutionary stage, smaller disks, such as HH212, L1527, and VLA 1623 W, should thus appear more settled than larger disks, such as IRAS04302, HL Tau, HD163296, Oph163131, which we do not observe.

Using the generic numerical values given by Sheehan et al. (2022), $\rho = 10^{-12} \text{ g cm}^{-3}$, $\rho_m = 3 \text{ g cm}^{-3}$, and $T = 50 \text{ K}$, we find that the settling timescale for grains of 1mm is $t_{\text{settle}, 100\text{au}} \sim 0.4 - 0.09 \text{ Myr}$ at 100au, and $t_{\text{settle}, 50\text{au}} \sim 0.05 - 0.01 \text{ Myr}$ at 50au, for $M_\star = 0.45 - 2M_\odot$. At 100au from the star, these estimates are comparable to the lifetime of Class 0 systems (0.13-0.26 Myr, Dunham et al. 2015; see also Kristensen & Dunham 2018). This suggests that, if they are located at 100au from the star, 1mm grains do not have time to settle at the Class 0 stage, while at 50au they are expected to settle before the end of the Class 0 stage. On the other hand, Class I objects have longer lifetimes (0.27-0.52 Myr, Dunham et al. 2015) and millimeter sized particles, if present, should already have totally settled both at 50au and 100au from the star.

Yet, we identify only a modest level of settling in IRAS04302, the only Class I of Table 4, and no evidence for settling in the small Class 0 and 0/I sources HH212, L1527, VLA 1623 W. This suggests that turbu-

Table 4. Stellar mass, outer radius, bolometric luminosity, accretion rate, evolutionary stage, and $[\alpha/St]_{100\text{au}}$ for 7 disks with constraints on their large dust height from ALMA observations.

	M_\star (M_\odot)	$R_{\text{out},\text{mm}}$ (au)	L_{bol} (L_\odot)	Accretion (M_\odot/yr)	Class	$[\alpha/St]_{100\text{au}}$	Dust Height	References
HH212	0.2-0.3	60	9.0	$2-4 \times 10^{-6}$	0	—	Vertically thick	1, 2, 3, 4
L1527	0.2-0.4	54	2.75	$5-11 \times 10^{-7}$	0/I	—	Vertically thick	5, 6, 7, 8
VLA 1623 W	0.45	50	0.13	2.5×10^{-8}	0/I	—	Vertically thick	9, 10, 11, 12
IRAS04302	1.6	300	0.15-0.67	$0.7-3 \times 10^{-8}$	I	$> 2 \times 10^{-2}$	$1\text{au} < H_{\text{ld},100\text{au}} < 6\text{au}$	This work, 13, 14
HL Tau	1.7	150	3.5-15	8.7×10^{-8}	I/II	—	$H_{\text{ld},100\text{au}} < 1\text{au}$	14, 15, 16
HD163296	2.0	240	—	4.5×10^{-7}	II	$< 1 \times 10^{-2}$	$H_{\text{ld},100\text{au}} < 1\text{au}$	17, 18, 19, 20, 21
Oph163131	1.2	150	—	—	II	$< 5 \times 10^{-3}$	$H_{\text{ld},100\text{au}} < 0.5\text{au}$	22, 23

NOTE—For HH212, L1527, VLA 1623 W, and IRAS04302, we recalculated the accretion rates based on their bolometric luminosity (see main text). For HD163296 and HL Tau, we report estimates based on the UV excess or HI recombination line luminosity. The outer radii and dust height correspond to the radial extent or dust height inferred for the dust detected at millimeter wavelengths with ALMA.

References—(1) Lee et al. (2014); (2) Codella et al. (2014); (3) Lee et al. (2017); (4) Lin et al. (2021); (5) Maret et al. (2020); (6) Tobin et al. (2008); (7) Sheehan et al. (2022); (8) Ohashi et al. (2022); (9) Mercimek et al. in prep; (10) Harris et al. (2018); (11) Murillo et al. (2018); (12) Michel et al. (2022); (13) Lin et al. in prep; (14) Robitaille et al. (2007); (15) Pinte et al. (2016); (16) Beck et al. (2010); (17) Teague et al. (2019); (18) Muro-Arena et al. (2018); (19) Mendigutía et al. (2013); (20) Doi & Kataoka (2021); (21) Liu et al. (2022); (22) Flores et al. (2021); (23) Villenave et al. (2022)

lence could be stronger in the earliest stages of star formation, preventing the dust grains to settle within the predicted timescale without turbulence. Interestingly, the values of α/St presented in Table 4 also indicate that, at 100au from the star, turbulence is stronger in the Class I IRAS04302 than in the Class II Oph163131 and HD163296. In addition, more evolved systems tend to have lower accretion rates (see Table 4) which would also be consistent with evolution of turbulence with time, even though accretion rate does not necessarily relates to the turbulence at 100au.

Alternatively, the difference in dust height between evolutionary classes might also be related to the difference in the environment external to the disk. Specifically, with an infalling envelope at the earliest stages of star formation, fresh grains are constantly being resupplied to the disk, both radially and vertically. So while the first grains to fall in may have had time to settle in the disk, recently added grains would not. Yet, recent studies showed that the grains falling onto the disk that are coming from the infalling envelope cannot have grown larger than a few 10s of microns, for timescale and density reasons (e.g., Silsbee et al. 2022), such that it is not clear if this effect would be sufficient to explain the thickness of young disks when observed at millimeter wavelengths. Further studies are needed in order to determine which mechanism is dominant in setting the apparent height of disks at millimeter wavelengths for different evolutionary stages.

6. CONCLUSIONS

We presented new VLA observations of the Class I IRAS04302 disk, at 5 different wavelengths between 6.8mm and 66mm. The disk is detected both at 6.8mm and 9.2mm, while processes other than dust continuum emission dominate the observations at 14mm, 40mm, and 66mm. We compare the disk size at centimeter wavelengths with its extent seen in millimeter ALMA observations at 0.9mm and 2.1mm and we find that the disk is about 70% smaller at 9.2mm than at 0.9mm. The spectral index maps obtained with the different millimeter and centimeter observations allow us to identify an increase of the spectral index with radius, from ~ 2 in the center to ~ 3 in the outer disk, consistent with the size difference observed in the images. We also find that the spectral index obtained when including the centimeter observations is consistently higher than the spectral index using only the 0.9mm and 2.1mm images (by about 0.5dex except at the center of the disk), indicating that the observations at 9.2mm and 6.8mm are more optically thin than the ALMA observations.

With the goal of characterizing the distribution of large dust in IRAS04302, we produced a grid of radiative transfer models aiming to reproduce the 0.9mm, 2.1mm, and 9.2mm data. The models implement one layer of large grains without substructures, and we determine the dust mass for each combination of parameters based on the major axis profiles at the three wavelengths previously mentioned. We show in Appendix B that adding

a small grain disk layer and envelope does not affect the shape of the millimeter/centimeter emission but allows to recover a more realistic temperature structure.

Our results indicate that if there are some grains of 1cm in the disk, they can not be well mixed with smaller dust particles and extend to the outer disk regions, because the emission would then appear too radially extended at 9.2mm. Such grains of 1cm might however be more concentrated radially than smaller grains, which can not be tested with the current data and modeling. Moreover, models with maximum grain sizes of $100\mu\text{m}$ or 1mm are able to reproduce the 0.9mm, 2.1mm, and 9.2mm major axis profiles simultaneously, which suggests that the apparent size difference between the millimeter and centimeter observations could be mostly due to optical depth effects. The models also favor a disk inclination very close to edge-on ($i > 88^\circ$). However, no clear trend was found for the different values of the surface density exponent p and the flaring exponent β tested within our grid.

Our modeling strategy also allows us to determine a plausible interval for the large dust scale height of $1\text{au} < H_{ld,100\text{au}} < 6\text{au}$. When compared to our estimate of the gas scale height $H_{g,100\text{au}} \sim 7\text{au}$, based on the midplane temperature profile of our best model, we identify that the millimeter dust in the disk is subject to at least moderate vertical settling. The level of settling in this Class I disk contrasts with previous results of Class 0 systems, where no settling is occurring, and of Class II disks, that are found to be thinner. By estimating the timescale of vertical settling for millimeter sized particles and comparing it to the lifetime of Class 0 and Class I systems, we suggest that this variation of set-

ling efficiency with time is linked to some variation of turbulence or of external conditions with time.

Acknowledgements: MV research was supported by an appointment to the NASA Postdoctoral Program at the (NASA Jet Propulsion Laboratory), administered by Oak Ridge Associated Universities under contract with NASA. EB acknowledges the Deutsche Forschungsgemeinschaft (DFG, German Research Foundation) under Germany's Excellence Strategy – EXC 2094 – 390783311. CC-G acknowledges support by UNAM DGAPA-PAPIIT grant IG101321 and CONACyT Ciencia de Frontera grant number 86372. GD acknowledges support from NASA grants 80NSSC18K0442 as well as NNX15AC89G and NNX15AD95G/NExSS. CC and LP acknowledge the EC H2020 research and innovation programme for the project "Astro-Chemical Origins" (ACO, No 811312) and the PRIN-MUR 2020 MUR BEYOND-2p (Astrochemistry beyond the second period elements, Prot. 2020AFB3FX). This paper makes use of the following ALMA data: ADS/JAO.ALMA#2016.1.00460.S. ALMA is a partnership of ESO (representing its member states), NSF (USA) and NINS (Japan), together with NRC (Canada), MOST and ASIAA (Taiwan), and KASI (Republic of Korea), in cooperation with the Republic of Chile. The Joint ALMA Observatory is operated by ESO, AUI/NRAO, and NAOJ.

Facilities: ALMA, VLA

Software: CASA (CASA Team et al. 2022), *mcfoast* (Pinte et al. 2006, 2009), *Matplotlib* (Hunter 2007), *Numpy* (Harris et al. 2020).

APPENDIX

A. CORRECTION FOR PROCESSES OTHER THAN DUST EMISSION

The variety of VLA observations allows us to perform a detailed analysis to remove emission from processes other than dust thermal emission (also referred to as non-dust or wind/coronal emission throughout the text) present at the center of the disk. To do so, we follow the approach highlighted in Carrasco-González et al. (2019). We first aligned the observations at the different wavelengths, using the CASA task *fixplanets*. Then, we produced an image combining the 66mm, 40mm, 14mm, and 6.8mm data together, aiming to model the non-dust emission of the disk. We use the *tclean* task with *nterm=2*, which allows us to obtain both the flux and

spectral index of the emission. We also assume a briggs robust parameter of 0 in order to be sensitive only to the brightest emission of the maps.

We note that at 6.8mm and 9.2mm it is possible that both dust and non-dust emission are present in the inner regions. To determine whether to use the 6.8mm or 9.2mm observations to model the wind/coronal emission, we looked at the shape of the emission when imaged with a robust briggs parameter of 0. First, we note that this parameter value was chosen to decrease the sensitivity of the imaging, such that only the brightest emission (expected to be from processes other than dust thermal emission) will be visible in the final image. In addition, we expect wind/coronal emission to

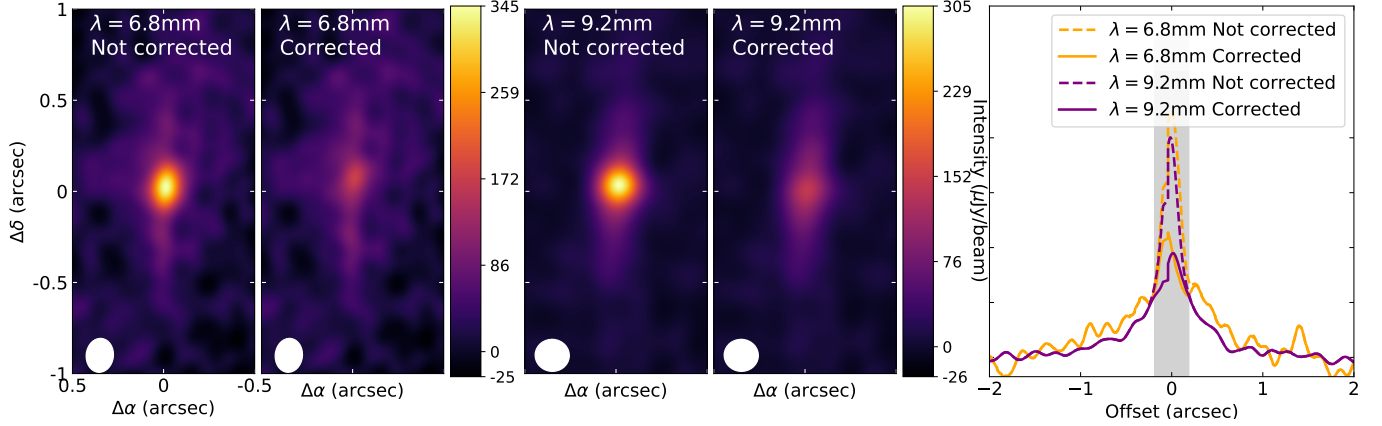


Figure 10. Resulting 6.8mm and 9.2mm images before (left panels) and after (middle panels) correction for non-disk emission, at the same angular and brightness scale. The right panel shows the major axis cut to the same brightness scale, illustrating that this correction only affects the central beam of the emission (marked with the filled grey region).

be concentrated within one beam, while dust emission from the disk should be more extended. We find that using a briggs 0 parameter the 6.8mm emission is concentrated within a central point source, and is thus likely dominated by processes other than dust thermal emission. On the contrary, with a briggs parameter of 0, the 9.2mm image is extended, meaning that it still contains substantial dust emission. Thus, we include the 6.8mm but not the 9.2mm observations in the non-dust model.

From the combined 66mm, 40mm, 14mm, and 6.8mm image, we find that the wind/coronal emission is unresolved, as expected. We obtain a model consisting of only one point, located at the center of the disk, and with a flux density of $150\mu\text{Jy}$ at 26 GHz, and a spectral index of $+0.46$, consistent with moderately optically thick free-free emission (Rodmann et al. 2006). This allows to predict the contribution from processes other than dust thermal emission at 9.2mm and 6.8mm, assuming that such emission did not vary significantly between October and December 2021.

To remove coronal/wind contamination from the 6.8mm and 9.2mm image, we then inserted the non-dust model images (combined 66mm, 40mm, 14mm, and 6.8mm image) into the 'model' column of the 6.8mm and 9.2mm visibilities using the `ft` task, and subtracted the model column from the data column using `uvsub`. Finally, we produced a model image using the parameters presented in Sect 2.1. We present the 6.8mm and 9.2mm images and major axis cut before and after correction in Fig. 10. These images clearly show that the correction significantly reduces the centrally peaked feature within 1 beam from the center, while keeping the outer regions unaffected. When modeling the disk (Sect. 4) we use the corrected 9.2mm image, but consider only the regions outside of 1 beam size to limit the effect of potential variability of wind/coronal emission.

B. SIMULTANEOUS MATCH OF THE THERMAL PART OF THE SED AND ALMA/VLA MAPS

Previous observations and modeling (Lucas & Roche 1997; Padgett et al. 1999; Wolf et al. 2003) found that the scattered light is dominated by an envelope. In Sect. 4, we have however omitted this part in order to save some computer power in the generation of our grid. In this Appendix, we show that including a disk layer of small grains and an envelope does not significantly affect the shape of the 0.89mm, 2.1mm, and 9.2mm observations. Our goal here is to produce a more realistic temperature structure of the disk that allows to match the millimeter fluxes and the thermal part of the Spectral Energy Distribution (SED, $\lambda \gtrsim 20\mu\text{m}$).

In order to obtain a better temperature structure of our disk, we thus add a disk layer of small grains and an envelope to the layer of large grains obtained as best model from our fitting methodology. We first added a layer of small grains with the parameters indicated in Table 5. Then, we tested a small number of envelope parameters. For simplicity, we assume that the envelope is spherically symmetric and that the density follows a power law in radius: $\rho \propto r^\gamma$. Following Wolf et al. (2003), we also include a cavity in our modeling. We assume that no dust is present above a surface represented by $z = z_0(r/r_0)^{\beta_{env}}$. We set the inner radius to 0.1au, the outer radius to 1000au, and varied the following parameters: $a_{max,env} \in [0.5, 1]$, $\gamma \in [-1, -2]$, $z_0 \in [1, 3, 5]$, and $M_{dust,env} \in [10^{-5}, 10^{-4}, 10^{-3}]$. Finally, we determined the best set of parameters based on a χ^2_{SED} estimate, using the SED match between 20 and $10000\mu\text{m}$ (7 points), and ϕ^2 of the 0.9mm observations only.

In Table 5, we show the resulting parameters for the small grain and envelope layers. We also include the comparison of the best big grains model ($H_d = 3\text{au}$, $i = 89^\circ$, $a_{max} = 1000\mu\text{m}$, $\beta=1.14$, $p = -1.5$, and

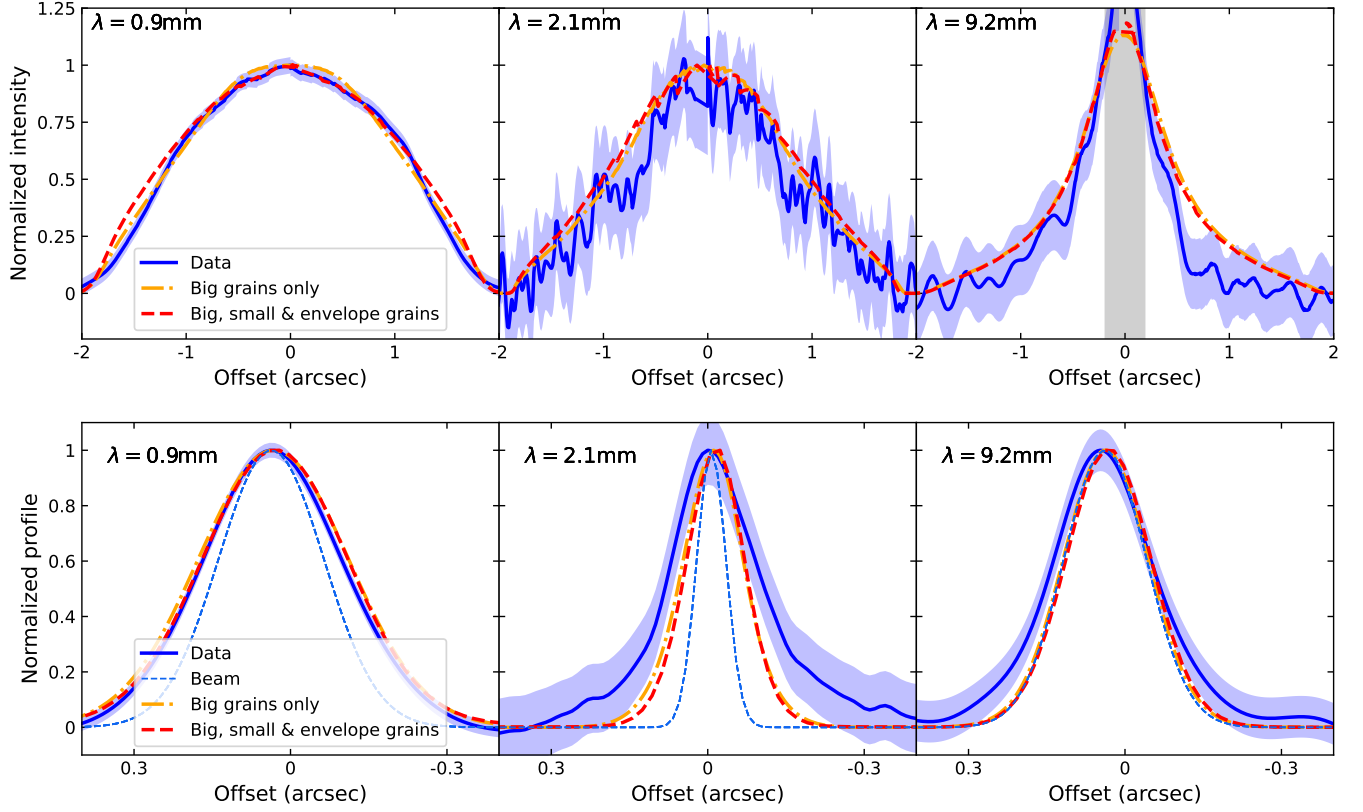


Figure 11. Comparison of the major axis profiles (top panels) and minor axis profiles (bottom panels) of the best model from Sect. 4.2.1 (in orange), that model plus an envelope and small grain layer (Table 5, in red), and the data (blue).

Table 5. Small grains layer and envelope parameters.

<i>Envelope & Cavity</i>		
$a_{min} - a_{max}$	(μm)	0.005 – 0.5
$R_{in} - R_{out}$	(au)	0.1 – 1000
M_{dust}	(M_{\odot})	$1 \cdot 10^{-5}$
γ	(–)	–2
z_0, r_0, β_{env}	(au, au, –)	5, 1, 1
<i>Small grains disk layer</i>		
$a_{min} - a_{max}$	(μm)	0.005 – 10
$R_{in} - R_{out}$	(au)	0.1 – 300
M_{dust}	(M_{\odot})	$5 \cdot 10^{-7}$
$H_{sd,100au}, \beta, p$	(au, –, –)	6.7, 1.14, –1

NOTE—The parameters for the small grain and envelope regions allow to produce a more realistic temperature structure of the disk than in Sect 4, but we emphasize that they are not expected to reproduce the previous scattered light observations and should not be considered as constraints on the envelope mass and shape.

$M_d = 0.0003M_{\odot}$) with or without including small grains and an envelope in Fig. 11 for the major and minor axis cut, and in Fig. 12 for the SED. As expected, we find that the thermal emission part of the model SED reproduces significantly better the data when a small grains

and envelope layers are included. On the other hand, no significant differences are found in the shape of the millimeter/centimeter emission between the two models. Most of the differences lie in the outer edges of the major axis profile at 0.9mm. This shows that, while the small grain and envelope layers are mostly invisible in the shape of the millimeter/centimeter observations, they contribute to obtain a more realistic disk structure and a larger total mm/cm flux, by allowing the midplane to be warmer. We emphasize that the parameters for the small grain and envelope region are not expected to reproduce the previous scattered light observations and should not be considered as constraints on the envelope mass and shape.

We find that adding the small grain and envelope layers allow to significantly increase the midplane temperature. At 100au from the central star, it goes from 11K with large grains only, to 21K when including the other layers. Using this midplane temperature value, it is possible to infer what is the gas scale height assuming that it is at the hydrostatic equilibrium, following:

$$H(r) = \sqrt{\frac{k_B T(r) r^3}{GM_{\star} \mu m_p}} \quad (B1)$$

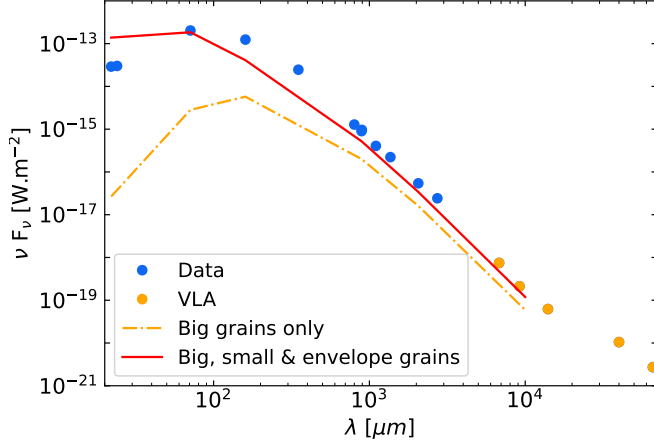


Figure 12. Comparison of the SED of the best model from Sect. 4.2.1 (in orange), that model plus an envelope and small grain disk layer (Table 5, in red), and the data (blue). The 6.8mm and 9.2mm VLA fluxes were corrected from processes other than dust emission.

where k_B is the Boltzmann constant, $\mu = 2.3$ the reduced mass, m_p the proton mass, G the gravitational constant. Using stellar mass of $M_\star = 1.6 M_\odot$ (Lin et al. in preparation), we find that the gas scale height of this disk is $H_{g,100au} \sim 7$ au.

C. ADDITIONAL MODEL COMPARISONS

C.1. Residual maps of the best model

We present the residual maps of the best model in Fig. 13. The parameters for the best model are: $H_{ld,100au} = 3au$, $i = 89^\circ$, $a_{max} = 1mm$, $\beta=1.14$, $p = 1.5$, and $M_{dust} = 3 \times 10^{-4} M_\odot$. We also note that the maps shown here do not have the small grain disk and envelope layer discussed in Appendix B.

C.2. Effect of p and i on a_{max}

While the maximum grain size has a clear impact on the shapes of the major axis profiles (Sect. 4.2.2, Fig. 7) it is possibly degenerated with three other parameters: M_{dust} , i , and p . In our first fitting step, we determine the best mass that allows to reproduce the major axis profile, thus the possible degeneracies between M_{dust} and a_{max} are already taken into account. In Fig. 14, we show the detailed $\bar{\chi}_{maj}^2$ median matrix for each combination of (a_{max}, i) and (a_{max}, p) . Both matrices show that independently of the value of i and p , $a_{max} = 1cm$ (lowest line) leads to significantly higher median $\bar{\chi}_{maj}^2$ values than lower maximum grain sizes. As indicated previously this implies that the maximum grain size in the system can not be 1cm in the outer regions of the disk and must be smaller.

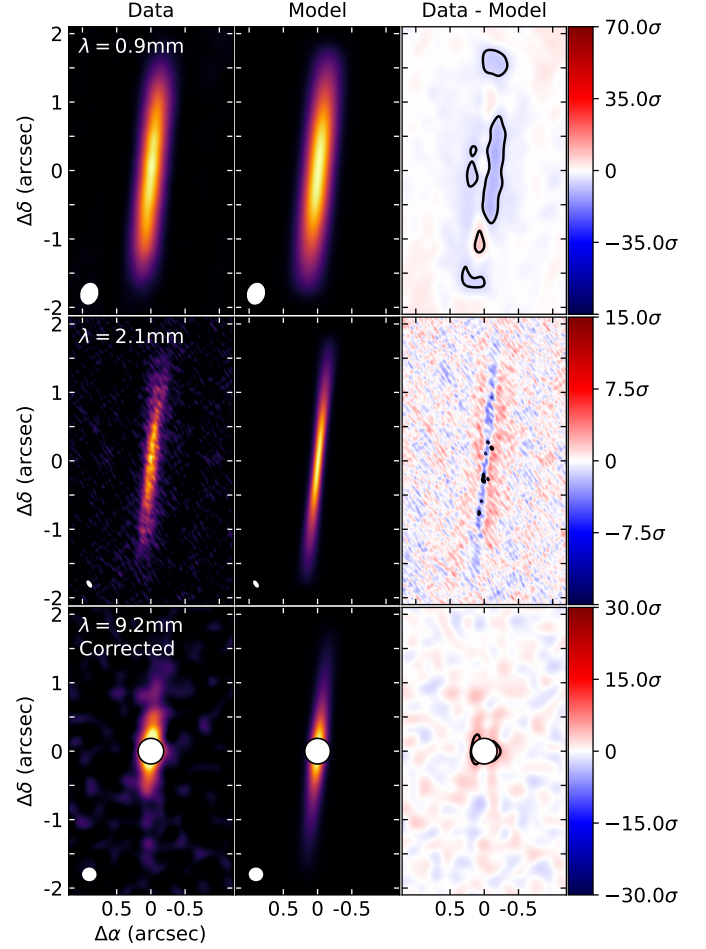


Figure 13. Left: Data images, Middle: Images of the best model, Right: Residual maps, with deviations by more than 5σ indicated by black contours. The central mask on the 9.2mm maps indicate the region potentially affected by coronal/wind emission that is not considered in our modeling.

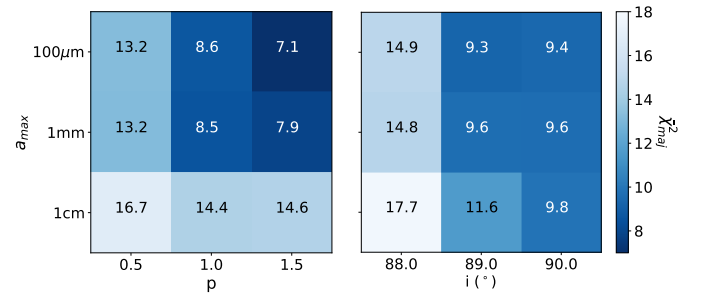


Figure 14. Median $\bar{\chi}_{maj}^2$ values for each combinations of (a_{max}, p) and (a_{max}, i) . Darker colors indicate smaller $\bar{\chi}_{maj}^2$, and thus a better combination of parameters.

For all a_{max} it is also clear that higher inclinations and higher surface density exponents are preferred ($i > 88^\circ$, and $p > 0.5$). This is because inclinations of 88° lead to models that are too centrally peaked. On the contrary,

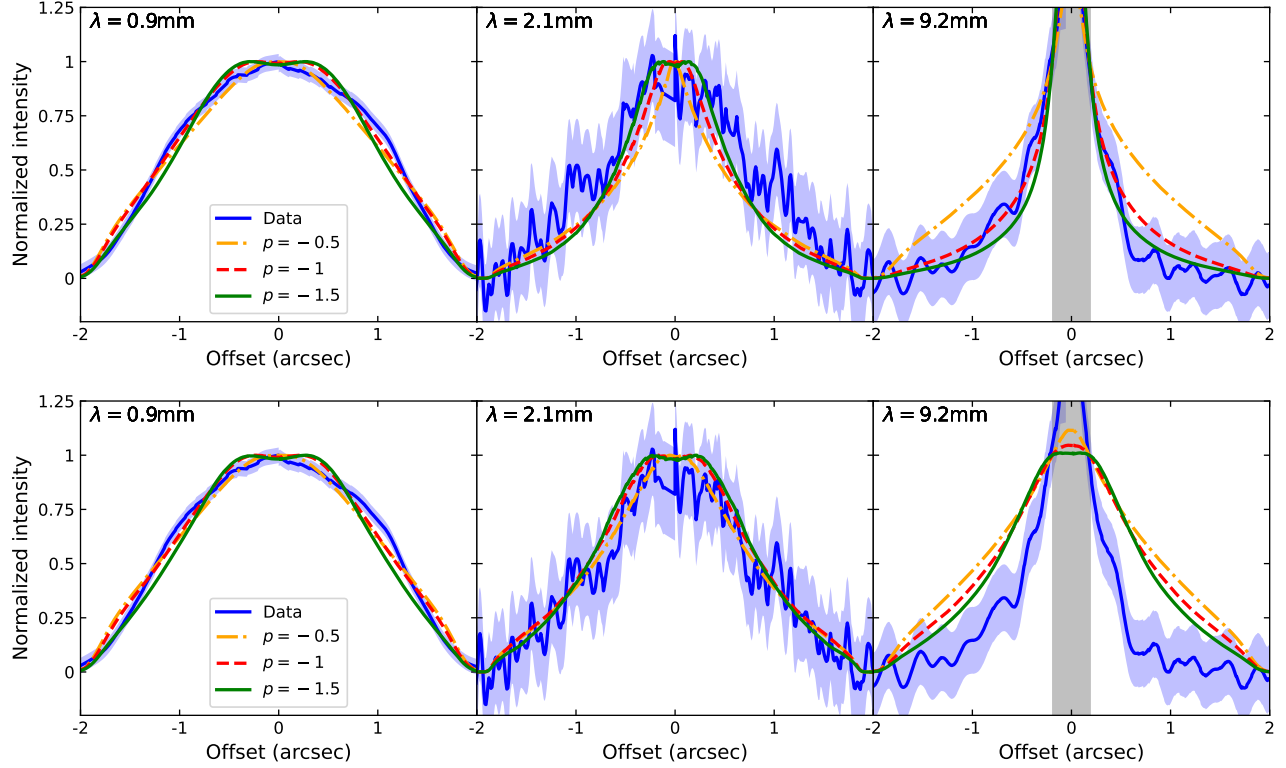


Figure 15. Effect of p on the major axis profiles, for $a_{max} = 100\mu\text{m}$ (top), and $a_{max} = 1\text{cm}$ (bottom).

surface density exponent of $p = 0.5$ implies a shallower radial profile, and leads the models to be too bright and radially extended at 9.2mm compared to the data. In Fig. 15, we show the effect of the surface density exponent on the shape of the major axis profiles, for a grain size of $a_{max} = 100\mu\text{m}$, and $a_{max} = 1\text{cm}$. For the lower maximum grain size ($a_{max} = 100\mu\text{m}$), low values of surface density exponents are more strongly excluded than when $a_{max} = 1\text{cm}$.

C.3. Effect of β and i on $H_{ld,100au}$

The models presented in Fig. 8 were computed for an inclination of $i = 90^\circ$ and flaring of $\beta = 1.14$. However,

both the inclination and the flaring exponent i and β can also impact the apparent minor axis size of the disk. In Fig. 16, we present the median ϕ^2 matrix for each combinations of $(H_{ld,100au}, i)$ and $(H_{ld,100au}, \beta)$. These maps (ϕ^2) show that larger inclinations and flaring are favored. Independently of the inclination and flaring exponent, we also find that a scale height of $H_{ld,100au} \sim 3\text{au}$ is favored.

REFERENCES

- Andre, P., Ward-Thompson, D., & Barsony, M. 2000, in Protostars and Planets IV, ed. V. Mannings, A. P. Boss, & S. S. Russell, 59.
<https://arxiv.org/abs/astro-ph/9903284>
- Andrews, S. M., Huang, J., Pérez, L. M., et al. 2018, ApJL, 869, L41, doi: [10.3847/2041-8213/aaf741](https://doi.org/10.3847/2041-8213/aaf741)
- Ansdell, M., Williams, J. P., Trapman, L., et al. 2018, ApJ, 859, 21, doi: [10.3847/1538-4357/aab890](https://doi.org/10.3847/1538-4357/aab890)
- Armitage, P. J. 2015, arXiv e-prints, arXiv:1509.06382.
<https://arxiv.org/abs/1509.06382>
- Barrière-Fouchet, L., Gonzalez, J. F., Murray, J. R., Humble, R. J., & Maddison, S. T. 2005, A&A, 443, 185, doi: [10.1051/0004-6361:20042249](https://doi.org/10.1051/0004-6361:20042249)
- Beck, T. L., Bary, J. S., & McGregor, P. J. 2010, ApJ, 722, 1360, doi: [10.1088/0004-637X/722/2/1360](https://doi.org/10.1088/0004-637X/722/2/1360)
- Carrasco-González, C., Sierra, A., Flock, M., et al. 2019, ApJ, 883, 71, doi: [10.3847/1538-4357/ab3d33](https://doi.org/10.3847/1538-4357/ab3d33)
- CASA Team, Bean, B., Bhatnagar, S., et al. 2022, PASP, 134, 114501, doi: [10.1088/1538-3873/ac9642](https://doi.org/10.1088/1538-3873/ac9642)



Figure 16. Median $\bar{\phi}^2$ for each combinations of (H_d, i) and (H_d, β) . Darker colors indicate smaller $\bar{\phi}^2$ and thus a better combination of parameters.

- Codella, C., Cabrit, S., Gueth, F., et al. 2014, *A&A*, 568, L5, doi: [10.1051/0004-6361/201424103](https://doi.org/10.1051/0004-6361/201424103)
- Doi, K., & Kataoka, A. 2021, *ApJ*, 912, 164, doi: [10.3847/1538-4357/abe5a6](https://doi.org/10.3847/1538-4357/abe5a6)
- Drazkowska, J., Bitsch, B., Lambrechts, M., et al. 2022, arXiv e-prints, arXiv:2203.09759. <https://arxiv.org/abs/2203.09759>
- Dullemond, C. P., Birnstiel, T., Huang, J., et al. 2018, *ApJL*, 869, L46, doi: [10.3847/2041-8213/aaf742](https://doi.org/10.3847/2041-8213/aaf742)
- Dunham, M. M., Allen, L. E., Evans, Neal J., I., et al. 2015, *ApJS*, 220, 11, doi: [10.1088/0067-0049/220/1/11](https://doi.org/10.1088/0067-0049/220/1/11)
- Flores, C., Duchêne, G., Wolff, S., et al. 2021, *AJ*, 161, 239, doi: [10.3847/1538-3881/abe1e](https://doi.org/10.3847/1538-3881/abe1e)
- Galli, P. A. B., Loinard, L., Bouy, H., et al. 2019, *A&A*, 630, A137, doi: [10.1051/0004-6361/201935928](https://doi.org/10.1051/0004-6361/201935928)
- Gräfe, C., Wolf, S., Guilloteau, S., et al. 2013, *A&A*, 553, A69, doi: [10.1051/0004-6361/201220720](https://doi.org/10.1051/0004-6361/201220720)
- Gullbring, E., Hartmann, L., Briceño, C., & Calvet, N. 1998, *ApJ*, 492, 323, doi: [10.1086/305032](https://doi.org/10.1086/305032)
- Harris, C. R., Millman, K. J., van der Walt, S. J., et al. 2020, *Nature*, 585, 357, doi: [10.1038/s41586-020-2649-2](https://doi.org/10.1038/s41586-020-2649-2)
- Harris, R. J., Cox, E. G., Looney, L. W., et al. 2018, *ApJ*, 861, 91, doi: [10.3847/1538-4357/aac6ec](https://doi.org/10.3847/1538-4357/aac6ec)
- Hunter, J. D. 2007, *Computing in Science and Engineering*, 9, 90, doi: [10.1109/MCSE.2007.55](https://doi.org/10.1109/MCSE.2007.55)
- Johansen, A., & Klahr, H. 2005, *ApJ*, 634, 1353, doi: [10.1086/497118](https://doi.org/10.1086/497118)
- Kenyon, S. J., & Hartmann, L. 1995, *ApJS*, 101, 117, doi: [10.1086/192235](https://doi.org/10.1086/192235)
- Kristensen, L. E., & Dunham, M. M. 2018, *A&A*, 618, A158, doi: [10.1051/0004-6361/201731584](https://doi.org/10.1051/0004-6361/201731584)
- Lee, C.-F. 2020, *A&A Rv*, 28, 1, doi: [10.1007/s00159-020-0123-7](https://doi.org/10.1007/s00159-020-0123-7)
- Lee, C.-F., Codella, C., Ceccarelli, C., & López-Sepulcre, A. 2022, *ApJ*, 937, 10, doi: [10.3847/1538-4357/ac8c28](https://doi.org/10.3847/1538-4357/ac8c28)
- Lee, C.-F., Hirano, N., Zhang, Q., et al. 2014, *ApJ*, 786, 114, doi: [10.1088/0004-637X/786/2/114](https://doi.org/10.1088/0004-637X/786/2/114)
- Lee, C.-F., Li, Z.-Y., Ho, P. T. P., et al. 2017, *Science Advances*, 3, e1602935, doi: [10.1126/sciadv.1602935](https://doi.org/10.1126/sciadv.1602935)
- Lin, Z.-Y. D., Lee, C.-F., Li, Z.-Y., Tobin, J. J., & Turner, N. J. 2021, *MNRAS*, 501, 1316, doi: [10.1093/mnras/staa3685](https://doi.org/10.1093/mnras/staa3685)
- Liu, Y., Bertrang, G. H. M., Flock, M., et al. 2022, *Science China Physics, Mechanics, and Astronomy*, 65, 129511, doi: [10.1007/s11433-022-1982-y](https://doi.org/10.1007/s11433-022-1982-y)
- Long, F., Pinilla, P., Herczeg, G. J., et al. 2018, *ApJ*, 869, 17, doi: [10.3847/1538-4357/aac8e1](https://doi.org/10.3847/1538-4357/aac8e1)
- Lucas, P. W., & Roche, P. F. 1997, *MNRAS*, 286, 895, doi: [10.1093/mnras/286.4.895](https://doi.org/10.1093/mnras/286.4.895)
- Maret, S., Maury, A. J., Belloche, A., et al. 2020, *A&A*, 635, A15, doi: [10.1051/0004-6361/201936798](https://doi.org/10.1051/0004-6361/201936798)
- Melis, C., Duchêne, G., Chomiuk, L., et al. 2011, *ApJL*, 739, L7, doi: [10.1088/2041-8205/739/1/L7](https://doi.org/10.1088/2041-8205/739/1/L7)
- Mendigutía, I., Brittain, S., Eiroa, C., et al. 2013, *ApJ*, 776, 44, doi: [10.1088/0004-637X/776/1/44](https://doi.org/10.1088/0004-637X/776/1/44)
- Michel, A., Sadavoy, S. I., Sheehan, P. D., Looney, L. W., & Cox, E. G. 2022, *ApJ*, 937, 104, doi: [10.3847/1538-4357/ac905c](https://doi.org/10.3847/1538-4357/ac905c)
- Murillo, N. M., Harsono, D., McClure, M., Lai, S. P., & Hogerheijde, M. R. 2018, *A&A*, 615, L14, doi: [10.1051/0004-6361/201833420](https://doi.org/10.1051/0004-6361/201833420)
- Muro-Arena, G. A., Dominik, C., Waters, L. B. F. M., et al. 2018, *A&A*, 614, A24, doi: [10.1051/0004-6361/201732299](https://doi.org/10.1051/0004-6361/201732299)
- Nakatani, R., Liu, H. B., Ohashi, S., et al. 2020, *ApJL*, 895, L2, doi: [10.3847/2041-8213/ab8eaa](https://doi.org/10.3847/2041-8213/ab8eaa)
- Ohashi, S., Nakatani, R., Liu, H. B., et al. 2022, *ApJ*, 934, 163, doi: [10.3847/1538-4357/ac794e](https://doi.org/10.3847/1538-4357/ac794e)
- Padgett, D. L., Brandner, W., Stapelfeldt, K. R., et al. 1999, *AJ*, 117, 1490, doi: [10.1086/300781](https://doi.org/10.1086/300781)
- Pinte, C., Dent, W. R. F., Ménard, F., et al. 2016, *ApJ*, 816, 25, doi: [10.3847/0004-637X/816/1/25](https://doi.org/10.3847/0004-637X/816/1/25)
- Pinte, C., Harries, T. J., Min, M., et al. 2009, *A&A*, 498, 967, doi: [10.1051/0004-6361/200811555](https://doi.org/10.1051/0004-6361/200811555)
- Pinte, C., Ménard, F., Duchêne, G., & Bastien, P. 2006, *A&A*, 459, 797, doi: [10.1051/0004-6361:20053275](https://doi.org/10.1051/0004-6361:20053275)
- Podio, L., Garufi, A., Codella, C., et al. 2020, *A&A*, 642, L7, doi: [10.1051/0004-6361/202038952](https://doi.org/10.1051/0004-6361/202038952)
- Robitaille, T. P., Whitney, B. A., Indebetouw, R., & Wood, K. 2007, *ApJS*, 169, 328, doi: [10.1086/512039](https://doi.org/10.1086/512039)
- Rodmann, J., Henning, T., Chandler, C. J., Mundy, L. G., & Wilner, D. J. 2006, *A&A*, 446, 211, doi: [10.1051/0004-6361:20054038](https://doi.org/10.1051/0004-6361:20054038)
- Rosotti, G. P., Teague, R., Dullemond, C., Booth, R. A., & Clarke, C. J. 2020, *MNRAS*, 495, 173, doi: [10.1093/mnras/staa1170](https://doi.org/10.1093/mnras/staa1170)

- Rota, A. A., Manara, C. F., Miotello, A., et al. 2022, *A&A*, 662, A121, doi: [10.1051/0004-6361/202141035](https://doi.org/10.1051/0004-6361/202141035)
- Sakai, N., Oya, Y., Higuchi, A. E., et al. 2017, *MNRAS*, 467, L76, doi: [10.1093/mnrasl/slx002](https://doi.org/10.1093/mnrasl/slx002)
- Sheehan, P. D., Tobin, J. J., Li, Z.-Y., et al. 2022, *ApJ*, 934, 95, doi: [10.3847/1538-4357/ac7a3b](https://doi.org/10.3847/1538-4357/ac7a3b)
- Silsbee, K., Akimkin, V., Ivlev, A. V., et al. 2022, *ApJ*, 940, 188, doi: [10.3847/1538-4357/ac978b](https://doi.org/10.3847/1538-4357/ac978b)
- Teague, R., Bae, J., & Bergin, E. A. 2019, *Nature*, 574, 378, doi: [10.1038/s41586-019-1642-0](https://doi.org/10.1038/s41586-019-1642-0)
- Tobin, J. J., Hartmann, L., Calvet, N., & D'Alessio, P. 2008, *ApJ*, 679, 1364, doi: [10.1086/587683](https://doi.org/10.1086/587683)
- van't Hoff, M. L. R., Harsono, D., Tobin, J. J., et al. 2020, *ApJ*, 901, 166, doi: [10.3847/1538-4357/abb1a2](https://doi.org/10.3847/1538-4357/abb1a2)
- Villenave, M., Ménard, F., Dent, W. R. F., et al. 2020, *A&A*, 642, A164, doi: [10.1051/0004-6361/202038087](https://doi.org/10.1051/0004-6361/202038087)
- Villenave, M., Stapelfeldt, K. R., Duchêne, G., et al. 2022, *ApJ*, 930, 11, doi: [10.3847/1538-4357/ac5fae](https://doi.org/10.3847/1538-4357/ac5fae)
- Weidenschilling, S. J. 1977, *MNRAS*, 180, 57, doi: [10.1093/mnras/180.2.57](https://doi.org/10.1093/mnras/180.2.57)
- Wolf, S., Padgett, D. L., & Stapelfeldt, K. R. 2003, *ApJ*, 588, 373, doi: [10.1086/374041](https://doi.org/10.1086/374041)
- Wolf, S., Schegerer, A., Beuther, H., Padgett, D. L., & Stapelfeldt, K. R. 2008, *ApJL*, 674, L101, doi: [10.1086/529188](https://doi.org/10.1086/529188)
- Wolff, S. G., Duchêne, G., Stapelfeldt, K. R., et al. 2021, *AJ*, 161, 238, doi: [10.3847/1538-3881/abeb1d](https://doi.org/10.3847/1538-3881/abeb1d)
- Youdin, A. N., & Lithwick, Y. 2007, *Icarus*, 192, 588, doi: [10.1016/j.icarus.2007.07.012](https://doi.org/10.1016/j.icarus.2007.07.012)
- Zhang, C.-P., Launhardt, R., Liu, Y., Tobin, J. J., & Henning, T. 2021, *A&A*, 646, A18, doi: [10.1051/0004-6361/202039536](https://doi.org/10.1051/0004-6361/202039536)